Bulletin of the Seismological Society of America, Vol. 94, No. 4, pp. 1557–1563, August 2004

Hybrid Modeling of Elastic *P-SV* Wave Motion: A Combined Finite-Element and Staggered-Grid Finite-Difference Approach

by Shuo Ma, Ralph J. Archuleta, and Pengcheng Liu

Abstract We present a new hybrid approach to simulate elastic *P-SV* wave propagation. The method combines a low-order finite-element method (FEM) with a fourth-order velocity–stress staggered-grid finite-difference method (FDM). The FEM is applied to boundaries such as the free surface and fault surface where the FDM has difficulty accounting for the boundary conditions. The FDM is used to propagate waves in the interior regions where the fourth-order staggered-grid FDM is more efficient than the FEM. A minimum of 12 and 6 points per wavelength are used in the regions modeled by the FEM and FDM, respectively. To couple the FDM and FEM, a strong interface, which is 3 or 4 finite-difference grid spacings wide, is constructed between the regions modeled by the FDM and FEM using a newly derived high-order interpolation scheme. The accuracy and efficiency of the interface and the new scheme were tested (1) by simulating a Lamb's problem and (2) by simulating a kinematic propagating rupture on a 45°-dipping fault. Comparisons of results with analytical solutions and those obtained using independent numerical methods show exceptional agreement. We show that in terms of efficiency and memory requirement the hybrid approach is comparable to the fourth-order velocity–stress staggered-grid FDM but greatly expands its applicability by providing an accurate method for dealing with complicated boundary conditions.

Introduction

Accurate modeling directly in the time domain of seismic-wave propagation in realistic geologic structures has been the focus in computational seismology for decades. The challenge is to develop high-performance methods that are capable of solving the elastic wave equation accurately while allowing one to deal with large and complicated computational domains as encountered in realistic applications.

For its simplicity, efficiency, and ease of implementation, the fourth-order velocity–stress staggered-grid finite-difference method (FDM) (Levander, 1988) has been most widely implemented (Frankel, 1993; Olsen *et al.*, 1995; Graves, 1996; Olsen and Archuleta, 1996; Pitarka and Irikura, 1996). It is second-order accurate in time and fourth-order accurate in space. By using effective material properties the FDM is able to deal with heterogeneous earth media fairly easily in a uniform grid (Moczo *et al.*, 2002). However, the FDM has difficulty implementing boundary conditions on complex geometric shapes. Significant difficulties arise in the presence of surface topography (Ohminato and Chouet, 1997) and in fault geometries that have little or no symmetry (Oglesby *et al.*, 1998). Most FDM simulations use a uniform grid. The grid size is determined by the slowest velocities in the model; these may span only a small portion of the model (usually the shallow sediments at or near the surface). Consequently the size of the numerical model increases dramatically with a smaller mesh size, making it impractical to model accurately the slowest velocity layers. Requiring velocities to be greater or equal to a specified threshold can cause significant errors in modeling surface waves (Day, 2002; Eisner and Clayton, 2002).

As the most popular method in the engineering community, the finite-element method (FEM) is recognized as a viable alternative to the FDM in the simulation of wave propagation (Lysmer and Drake, 1972; Toshinawa and Ohmachi, 1992; Bao *et al.*, 1998). The FEM allows the use of irregular grids with elements of different size, geometry, and order of approximations. These advantageous features make it very efficient not only to treat boundary conditions sufficiently accurately, but also to resolve naturally the multiscale velocity structures. The unstructured grid FEM has been successfully applied to the study of wave propagation in 3D heterogeneous sedimentary basins (Bao *et al.*, 1998) and is regarded as likely the most accurate scheme for being able to sample the high-velocity gradient near the surface (Day, 2002). However, there are some major disadvantages with the FEM. First, it is not easily implemented. The mesh generation process can be complicated and can require significant computation time in its own right. The quality of the

mesh is critical to the success of the simulation. Secondly, the global stiffness matrix, which needs be formed and stored, requires significantly more memory than the FDM. For instance, in a cubic-element structured-grid 3D FEM simulation, each node has 81 stiffness terms, whereas each FDM grid stores only three material constants. To reduce the memory requirement, an element-by-element scheme can be used (Cook *et al.*, 2002). However, the temporal efficiency is reduced because the internal forces (in fact, local stiffness matrices) are recomputed at every timestep.

The spectral element method (SEM) has recently gained interest among seismologists (Komatitsch and Vilotte, 1998; Komatitsch and Tromp, 1999, 2002a,b). It is essentially a high-order FEM with the aforementioned advantages and disadvantages of the FEM. The uniqueness of the SEM is that the spatial discretization is based on the Legendre polynomials and Gauss–Lobatto–Legendre techniques that lead to a diagonal mass matrix. However, because SEM is a higher-order FEM with a minimum of five nodes per wavelength (Komatitsch and Vilotte, 1998), the number of neighboring nodes for each node is inevitably much larger than that in the low-order FEM. Consequently the number of CPU operations per timestep is much higher than the low-order FEM.

One way to keep advantages of both the FDM and the low-order FEM methods is to combine the FDM with the FEM. Moczo *et al.* (1997) presented a combined finite-element and finite-difference method to compute the *P-SV* seismic motion for inhomogeneous viscoelastic topographic structures. The efficiency is greatly increased compared to using the FEM alone in terms of saving memory and reducing mesh generation effort. However, their hybrid method was based on a second-order regular-grid displacement FDM and a low-order FEM. Both methods require at least 10 grids per minimum wavelength for accuracy. We have derived the FEM formulas in a uniform finite-element mesh in a very similar form of a regular-grid FDM (see the Appendix).

In this article, we present a combined FEM and fourth-order velocity–stress staggered-grid FDM. We use the FEM for critical boundaries and the fourth-order velocity–stress staggered-grid FDM as the principal means of propagating waves in the volume. In the following sections, we first present a new interface between the fourth-order velocity–stress staggered-grid FDM and the FEM and outline the algorithm of the combined approach. To test the accuracy and efficiency of the scheme, we compare our numerical solutions with analytical solutions or numerical solutions obtained by independent methods. We show results for a Lamb's problem in a homogeneous half-space and for a prescribed kinematic rupture propagation in a layered medium.

The FDM and FEM Interface

In this article, our FEM schemes follow closely the standard FEM implementations for dynamical problems (Cook *et al.*, 2002) by using second-order elements, such as 3-node triangles and 4-node rectangles. The mass matrix is lumped. The FEM equation is solved by using a central-difference approximation. Our FDM scheme is the standard fourth-order velocity–stress staggered-grid FDM; see Levander (1988), Graves (1996), and Moczo (1998) for details.

In the hybrid approach, the FDM and FEM algorithms have to communicate at the contact of the two corresponding computational regions during the entire process of time integration. Different from the combination of the FEM and regular-grid displacement FDM (Moczo *et al.*, 1997), where the interface between the FEM and FDM is 1 FDM grid-spacing wide, we find that the interface has to be 3 or 4 FDM grid-spacings wide in a combination with the fourth-order staggered-grid FDM to keep the fourth-order accuracy near the contact regions in the FDM. Figure 1 shows such an interface. The shaded area is overlapped by the FDM and FEM grids. Because we use 6 and 12 grid points per minimum wavelength in the FDM and FEM regions, respectively, the finite elements in the overlapped area are square elements with element size equal to half the FDM grid size. Nodes on line A are internal for the FDM (Fig. 1). At the same time, they are the boundary nodes for the FEM region. Similarly, the grid points in the overlapped area are the boundary grids for the FDM, but also the interior nodes for the FEM region. In this way, the FDM and FEM communicate with each other. Stresses within the interface are necessary to update the velocities near line A in the FDM. We compute the stresses within the interface using the FDM instead of the FEM. In

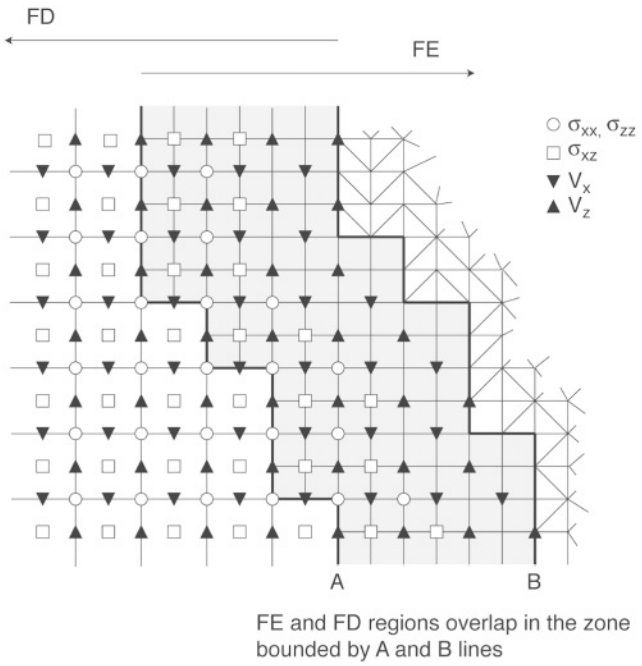

Figure 1. A general interface between a fourth-order velocity-stress staggered-grid finite-difference and a second-order finite-element grids. The interface is covered by both the finite-difference and finite-element grids. The overlap region has to be 3 or 4 FDM grid spacings wide to maintain accuracy.

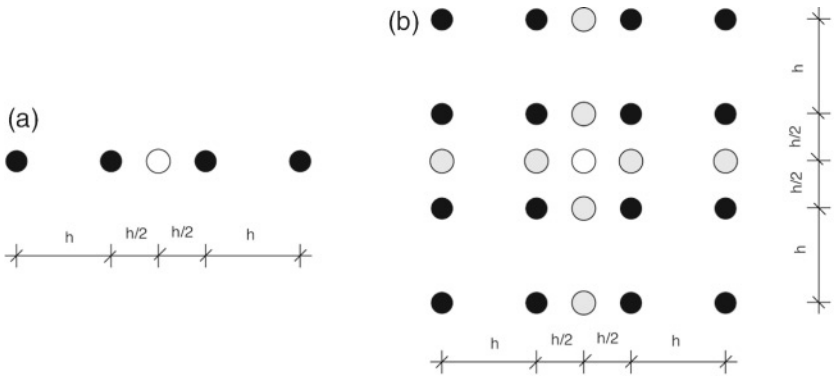

Figure 2. Illustration of the interpolation scheme. Solid circles denote known values. Gray circles denote intermediate values. Open circles are values to be determined. h is the FDM grid spacing. (a) Interpolation for 1D data; (b) interpolation for 2D data.

the FDM stresses have the same order accuracy as the velocities, but 1 order lower accuracy than the displacements (or velocities) in the FEM.

The time integration procedure is summarized in the following steps:

1. Calculate velocities at time level $m + 1/2$ from those at time level $m - 1/2$ and stresses at time level m in the FDM region (to the left of line A, including line A).
2. Calculate displacements at time level $m + 1$ from those at time levels $m - 1$ and m in the FEM region (excluding line A). Using the displacements at time levels m and $m + 1$ calculate the velocities at $m + 1/2$ at the FEM nodes in the overlapped area; next, assign to them the appropriate FDM velocity grids in the overlapped area. At this point, all the velocities in the whole FDM region are calculated.
3. Update the stresses at time level $m + 1$ from those at time level m and velocities at time level $m + 1/2$ in the whole FDM region.
4. Use a special interpolation scheme (discussed in the next paragraph) to get the velocities at FEM nodes on line A at time level $m + 1/2$. Calculate the displacements on line A at time level $m + 1$ using the displacements at time level m and velocities at time level $m + 1/2$. All the displacements in the FEM region are now calculated, and we restart the process.

Interpolating velocities on the finite-difference grids to get velocities on the finite-element nodes (line A in Fig. 1) is critical to the accuracy and stability of the hybrid method. A linear interpolation scheme fails to generate accurate results in our tests. However, higher-order interpolations might cause instability. Assuming the velocity field is a third-order polynomial, we have derived a new interpolation scheme. Because we always interpolate to get the velocities at a midpoint, we use

$$V_0 = \frac{9}{16}(V_{-1} + V_1) - \frac{1}{16}(V_{-2} + V_2), \qquad (1)$$

where V_0, V_{-1}, V_1, V_{-2}, and V_2 are shown in Figure 2a. Similarly, to interpolate a velocity in the center of a regular grid cell (Fig. 2b), we use equation (1) to get velocities in either a horizontal or vertical direction. Then we do the interpolation again to get the value in the center.

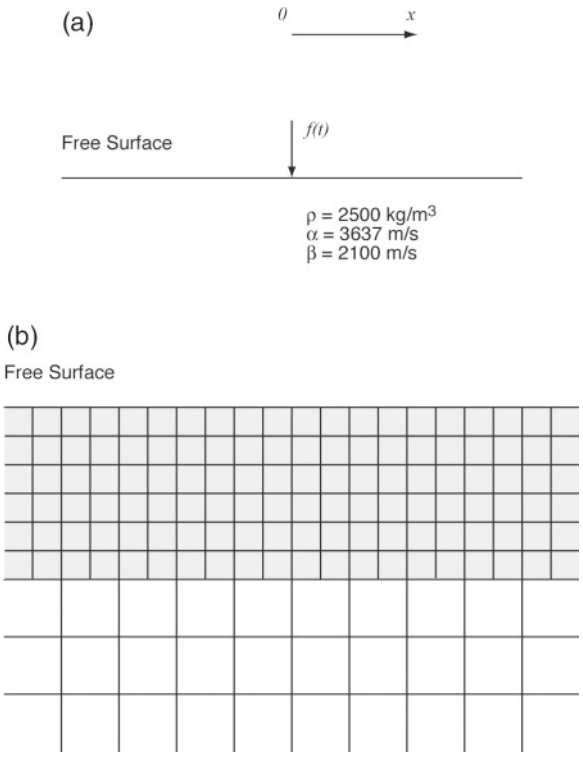

Figure 3. Model for Lamb's problem: (a) Upper diagram shows geometry; (b) lower panel shows part of the spatial grid with the free surface above the shaded area—a transition zone between the finite-element and finite-difference girds.

Numerical Tests

To test the accuracy of our method, especially the FDM–FEM interface, we compare numerical results for selected problems with results obtained by independent methods of calculation. In the following calculations the regular-shaped interfaces are used for simplicity. No absorbing boundaries are used in these tests. The model boundaries are simply put

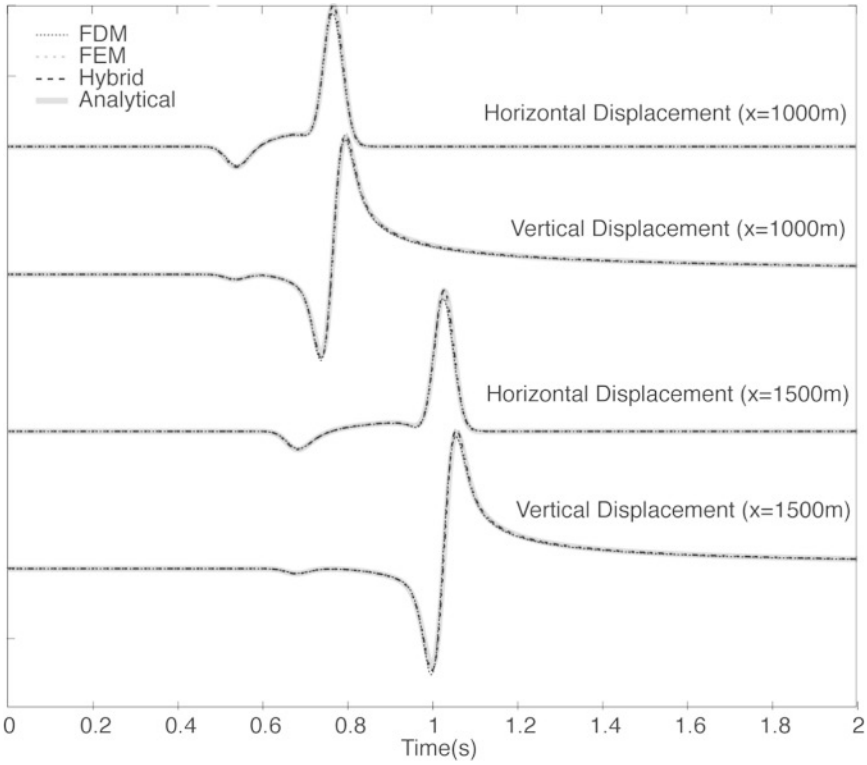

Figure 4. Comparison of the analytical solution for Lamb's problem with numerical solutions calculated by the FDM, FEM, and our hybrid approach. The FEM solution (short dashed line), and FDM solution (dotted line), and hybrid solution (long dashed line) show excellent agreement with the analytical solution (thick gray line).

far from the region of interest such that reflections arrive after the time of interest.

Lamb's Problem

Lamb's (1904) problem provides a stringent test for the accuracy of the numerical approximation of the free-surface boundary conditions. We apply a vertical point force at the free surface of a homogeneous half-space. The geometry of the physical problem is shown in Figure 3a. The force is a narrowbanded Gaussian type of pulse with the functional form $f(t) = \exp[-1000(t - 0.25)^2]$. The analytical solution is calculated using the Cagniard–de Hoop technique (de Hoop, 1960) and convolved numerically with the source time function.

In our numerical simulation, we apply a uniform square finite-element mesh in a narrow strip extending along the free surface and the finite-difference grid for the interior region. The interface is 3 finite-difference grid spacings wide (Fig. 3b). The solutions are calculated up to 35 Hz; they are compared with the analytical solution and independent FDM and FEM solutions. The FDM and FEM solutions are obtained with the standard fourth-order velocity–stress staggered-grid FDM and a uniform square-mesh FEM, respectively. This applies to the FDM and FEM solutions in the following example as well. All computation parameters are listed in Table 1. Waveform comparisons are seen in Figure 4. The direct P wave, S wave, and nondispersive Rayleigh wave are clearly seen. The FEM solution, the FDM solution, and our hybrid solution match the analytical solutions almost perfectly. As seen in Table 1, our hybrid approach takes much less calculation time than the FEM but is about as efficient as the FDM.

Inclusion of an Earthquake Fault

In our second example, we include a 45°-dipping fault in a one-layered velocity model. The geometry of the model is shown in Figure 5a. The slip function S has the same shape and amplitude everywhere on the fault but is time shifted by an amount proportional to the distance from the hypocenter as determined by a constant rupture velocity v_{rup} of 3000 m/sec. The functional form of S is given by

$$S(\tau) = S_0\,[1 - (1 + \tau/T)\exp(-\tau/T)]H(\tau),$$

where H is the Heaviside step function, τ is the time of the rupture arrival, S_0 is the static slip (1 m), and T is the rise time (0.1 sec).

In our hybrid modeling, the structured finite-element mesh covers the region that includes the whole fault. The remainder of the model is covered by a finite-difference grid, including the free surface and the layer interface in this example. The FDM–FEM interface surrounds the FEM region.

Table 1
Lamb's Problem: Computation Parameters and CPU Hours

	FDM	FEM	Hybrid	
Model dimensions ($nx \times nz$)	1000 × 400	2000 × 800	2000 × 6 (FEM)	1000 × 400 (FDM)
Grid spacing (m)	10	5	5	10
Time step (sec)	0.00125	0.00125	0.00125	
Duration (sec)	2	2	2	
Max frequency (Hz)	35	35	35	
Run time (hours) (UltraSparc 30)	~3–4	~9	~3–4	

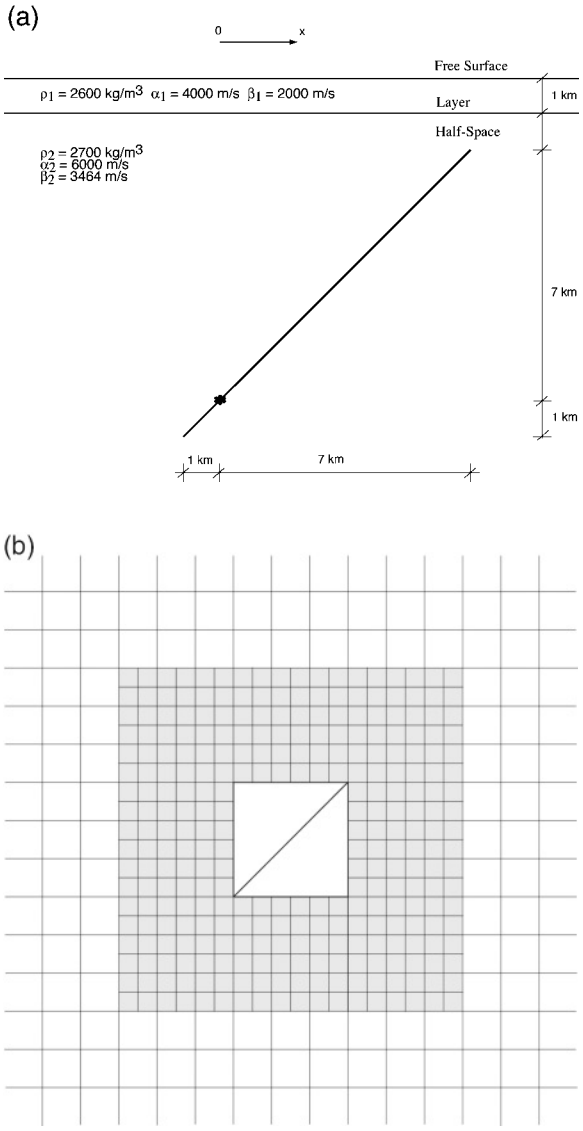

Figure 5. Model of a 45° dipping fault in a layered medium: (a) Geometry of the problem; (b) part of the spatial grid showing the interface (shaded area) between the finite-element and finite-difference grids. For illustration purposes, the fault length is dramatically shortened and the finite-element mesh within the surrounding box (which is too fine to draw) is not shown. Even the uniform finite-difference grid is much denser in the actual simluation. The free surface and the layer interface are not shown.

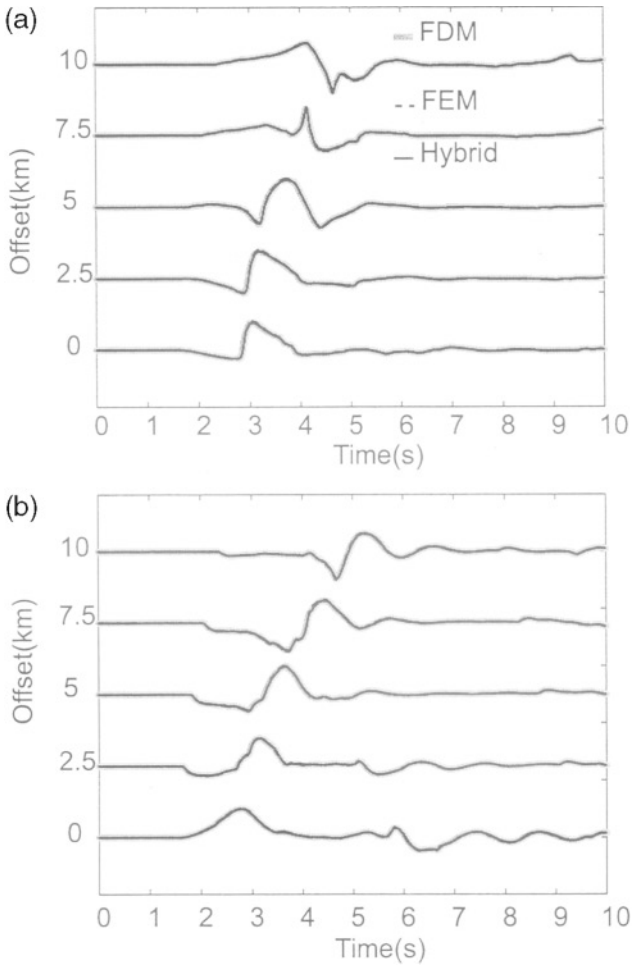

Figure 6. Comparision of seismograms calculated with FDM, FEM, and our hybrid method for different offsets caused by a prescribed rupture propagation on a 45° dipping fault shown in Figure 5. Each pair is normalized independently. In the upper panel (a) the horizontal component is shown; in the lower panel (b) the vertical component is shown. The hybrid solutions (thin solid line) are very consistent with the FDM and the FEM.

The finite-difference grid spacing size is twice the size used in the FEM (Fig. 5b). The time histories of particle velocity are calculated at the surface up to a maximum frequency 6.67 Hz. The results are compared with individual FDM and FEM solutions in Figure 6. The hybrid solutions agree very

Table 2
Kinematic Rupture: Computation Parameters and CPU Hours

	FDM	FEM	Hybrid	
Model dimensions ($nx \times nz$)	800 × 600	1600 × 1200	332 × 332 (FEM)	800 × 600 (FDM)
Grid spacing (m)	50	25	25	50
Time step (sec)	0.005	0.004	0.004	
Duration (sec)	10	10	10	
Max frequency (Hz)	6.67	6.67	6.67	
Run time (hours) (UltraSparc 30)	~1–2	~6–7	~2–3	

well with the FDM solutions and the FEM solutions. The excellent agreement demonstrates the highly accurate modeling of the interface between the FDM and FEM. In Table 2 we list the parameters and CPU times for each simulation. Again the hybrid method is much more efficient than the FEM and comparable to the FDM for these 2D computations.

Conclusions

We have presented a new interface in our hybrid approach for calculating *P-SV* wave propagation that can be used for realistic geological structures. The hybrid method is based on a combination of the fourth-order staggered-grid FDM and second-order FEM. We have shown that our method has the efficiency of the staggered-grid FDM while keeping the flexibility of the FEM. The interface between the finite element and the finite difference has been shown to be highly accurate and efficient. The same technique can be easily extended to 3D, which will accentuate the efficiency compared to 3D FEM. Special mapping between the FDM and FEM might be needed in complicated cases. But it can be done by implementing a new mesh generator, which can generate FEM mesh and FDM grids at the same time. The mapping between the FEM nodes and FDM grids around the FDM–FEM interface can then be easily realized in the mesh generator. The hybrid approach should be particularly useful in the simulation of strong ground motion where surface topography, complex subsurface geology, and complex fault geometry have to be taken into account.

Acknowledgments

We are very grateful to Jacobo Bielak, Peter Moczo, and Jozef Kristek for constructive discussions on the numerical methods. Many thanks to Eric Dunham for providing the analytical solutions for the Lamb's problem. This work has been supported by the W. M. Keck Foundation grant to UCSB for an interdisciplinary program in seismology and materials physics, the NSF/USGS Southern California Earthquake Center, and NSF Grant EAR-0073899. This is ICS Contribution Number 0577.

References

Bao, H., J. Bielak, O. Ghattas, L. F. Kallivokas, D. R. O'Hallaron, J. R. Shewchuk, and J. Xu (1998). Large-scale simulation of elastic wave propagation in heterogeneous media on parallel computers, *Comput. Methods Appl. Mech. Eng.* **152,** 85–102.

Cook, R. D., D. S. Malkus, M. E. Plesha, and R. J. Witt (2002). *Concepts and Applications of Finite Element Analysis*, Fourth Ed., Wiley, New York.

Day, S. M. (2002). Tests of 3D elastodynamic codes, final report to the Pacific Earthquake Engineering Research Center, Richmond, California.

de Hoop, A. T. (1960). A modification of Cagniard's method for solving seismic pulse problems, *Appl. Sci. Res.* **B8,** 349–356.

Eisner, L., and R. W. Clayton (2002). Equivalent medium parameters for numerical modeling in media with near-surface low velocities, *Bull. Seism. Soc. Am.* **92,** 711–722.

Frankel, A. (1993). Three-dimensional simulations of ground motions in San Bernardino Valley, California, for hypothetical earthquakes on the San Andreas fault, *Bull. Seism. Soc. Am.* **93,** 1020–1041.

Graves, R. W. (1996). Simulating seismic wave propagation in 3D elastic media using staggered-grid finite differences, *Bull. Seism. Soc. Am.* **86,** 1091–1106.

Komatitsch, D., and J. Tromp (1999). Introduction to the spectral-element method for 3-D seismic wave propagation, *Geophys. J. Int.* **139,** 806–822.

Komatitsch, D., and J. Tromp (2002a). Spectral-element simulations of global seismic wave propagation—I. Validation, *Geophys. J. Int.* **149,** 390–412.

Komatitsch, D., and J. Tromp (2002b). Spectral-element simulations of global seismic wave propagation—II. 3-D models, oceans, rotation, and self-gravitation, *Geophys. J. Int.* **150,** 303–318.

Komatitsch, D., and J. P. Vilotte (1998). The spectral-element method: an efficient tool to simulate the seismic response of 2D and 3D geological structures, *Bull. Seism. Soc. Am.* **88,** 368–392.

Lamb, H. (1904). On the propagation of tremors over the surface of an elastic solid, *Phil. Trans. R. Soc. London A* **203,** 1–42.

Levander, A. R. (1988). Fourth-order finite-difference *P-SV* seismograms, *Geophysics* **53,** 1425–1436.

Lysmer, J., and L. A. Drake (1972). A finite element method for seismology, *in Methods in Computational Physics*, Vol. 11, Academic, New York.

Moczo, P. (1998). Introduction to modeling seismic wave propagation by the finite-difference method, lecture notes at Disaster Prevention Research Institute, Kyoto University, 1997.

Moczo, P., E. Bystricky, J. Kristek, J. Carcione, and M. Bouchon (1997). Hybrid modeling of *P-SV* seismic motion at inhomogeneous viscoelastic topographic structures, *Bull. Seism. Soc. Am.* **87,** 1305–1323.

Moczo, P., J. Kristek, V. Vavrycuk, R. J. Archuleta, and L. Halada (2002). 3D heterogeneous staggered-grid modeling of seismic motion with volume harmonic and arithmetic averaging of elastic moduli and densities, *Bull. Seism. Soc. Am.* **92,** 3042–3066.

Ogelsby, D. D., R. J. Archuleta, and S. B. Nielsen (1998). Earthquakes on dipping faults: the effects of broken symmetry, *Science* **280,** 1055–1059.

Ohminato, T., and B. A. Chouet (1997). A free-surface boundary condition for including 3D tompography in the finite-difference method, *Bull. Seism. Soc. Am.* **87,** 494–515.

Olsen, K. B., and R. J. Archuleta (1996). Three-dimensional simulation of earthquakes on the Los Angeles fault system, *Bull. Seism. Soc. Am.* **86,** 575–596.

Olsen, K. B., R. J. Archuleta, and J. Matarese (1995). Magnitude 7.75 earthquake on the San Andreas fault: three-dimensional ground motion in Los Angles, *Science* **270,** 1628–1632.

Pitarka, A., and K. Irikura (1996). Basin structure effects on long-period strong motions in the San Fernando Valley and the Los Angles basin from the 1994 Northridge earthquake and aftershocks, *Bull. Seism. Soc. Am.* **96,** S126–S137.

Toshinawa, T., and T. Ohmachi (1992). Love wave propagation in three-dimensional sedimentary basin, *Bull. Seism. Soc. Am.* **82,** 1661–1667.

Appendix

In a uniform finite-element mesh for a *P-SV* problem in a homogeneous medium, after lumping the mass matrix, calculating the stiffness matrix, and summing the stiffness contributions over neighboring elements for an interior node, the displacement at this node can be updated in a regular-grid finite-difference fashion. It is derived as follows:

$$
\begin{aligned}
U_{i,j}^{m+1} &= 2U_{i,j}^{m} - U_{i,j}^{m-1} + \frac{\Delta t^2}{\rho h^2} F_{i,j}^{x,m} \\
&- \frac{\Delta t^2}{\rho h^2}\left[- \frac{\lambda + 3\mu}{6} U_{i-1,j-1}^{m} - \frac{\lambda + \mu}{4} V_{i-1,j-1}^{m} \right. \\
&+ \frac{\lambda}{3} U_{i-1,j}^{m} - \frac{\lambda + 3\mu}{6} U_{i-1,j+1}^{m} + \frac{\lambda + \mu}{4} V_{i-1,j+1}^{m} \\
&- \left(\frac{2}{3}\lambda + \mu\right) U_{i,j-1}^{m} + \frac{4}{3}(\lambda + 3\mu) U_{i,j}^{m} - \left(\frac{2}{3}\lambda + \mu\right) U_{i,j+1}^{m} \\
&- \frac{\lambda + 3\mu}{6} U_{i+1,j-1}^{m} + \frac{\lambda + \mu}{4} V_{i+1,j-1}^{m} + \frac{\lambda}{3} U_{i+1,j}^{m} \\
&\left. - \frac{\lambda + 3\mu}{6} U_{i+1,j+1}^{m} - \frac{\lambda + \mu}{4} V_{i+1,j+1}^{m} \right]
\end{aligned}
$$

$$
\begin{aligned}
V_{i,j}^{m+1} &= 2V_{i,j}^{m} - V_{i,j}^{m-1} + \frac{\Delta t^2}{\rho h^2} F_{i,j}^{z,m} \\
&- \frac{\Delta t^2}{\rho h^2}\left[- \frac{\lambda + \mu}{4} U_{i-1,j-1}^{m} - \frac{\lambda + 3\mu}{6} V_{i-1,j-1}^{m} \right. \\
&- \left(\frac{2}{3}\lambda + \mu\right) V_{i-1,j}^{m} + \frac{\lambda + \mu}{4} U_{i-1,j+1}^{m} - \frac{\lambda + 3\mu}{6} V_{i-1,j+1}^{m} \\
&+ \frac{\lambda}{3} V_{i,j-1}^{m} + \frac{4}{3}(\lambda + 3\mu) V_{i,j}^{m} + \frac{2}{3} V_{i,j+1}^{m} \\
&+ \frac{\lambda + \mu}{4} U_{i+1,j-1}^{m} + \frac{\lambda + 3\mu}{6} V_{i+1,j-1}^{m} - \left(\frac{2}{3}\lambda + \mu\right) V_{i+1,j}^{m} \\
&\left. - \frac{\lambda + \mu}{4} U_{i+1,j+1}^{m} - \frac{\lambda + 3\mu}{6} V_{i+1,j+1}^{m} \right],
\end{aligned}
$$

where U and V are the horizontal and vertical displacement; F is the external force; Δt is the time step; i and j are the spatial indexes in the horizontal (x) and vertical (z) direction, respectively; m is the temporal index; h is the element size; ρ is the density; γ and μ are Lame's constants.

Similarly, for a grid point at the free surface, the displacement can be updated as

$$
\begin{aligned}
U_{0,j}^{m+1} &= 2U_{0,j}^{m} - U_{0,j}^{m-1} + \frac{\Delta t^2}{0.5\rho h^2} F_{0,j}^{x,m} \\
&- \frac{\Delta t^2}{0.5\rho h^2}\left[- \frac{2\lambda + 3\mu}{6} U_{0,j-1}^{m} - \frac{\lambda + \mu}{4} V_{0,j-1}^{m} \right. \\
&+ \frac{2}{3}(\lambda + 3\mu) U_{0,j}^{m} - \frac{2\lambda + 3\mu}{6} U_{0,j+1}^{m} + \frac{\lambda - \mu}{4} V_{0,j+1}^{m} \\
&- \frac{\lambda + 3\mu}{6} U_{1,j-1}^{m} + \frac{\lambda + \mu}{4} V_{1,j-1}^{m} + \frac{\lambda}{3} U_{1,j}^{m} \\
&\left. - \frac{\lambda + 3\mu}{6} U_{1,j+1}^{m} - \frac{\lambda + \mu}{4} V_{1,j+1}^{m} \right]
\end{aligned}
$$

$$
\begin{aligned}
V_{0,j}^{m+1} &= 2V_{0,j}^{m} - V_{0,j}^{m-1} + \frac{\Delta t^2}{0.5\rho h^2} F_{0,j}^{z,m} \\
&- \frac{\Delta t^2}{0.5\rho h^2}\left[\frac{\lambda - \mu}{4} U_{0,j-1}^{m} + \frac{\lambda}{6} V_{0,j-1}^{m} \right. \\
&+ \frac{2}{3}(\lambda + 3\mu) V_{0,j}^{m} - \frac{\lambda - \mu}{4} U_{0,j+1}^{m} + \frac{\lambda}{6} V_{0,j+1}^{m} \\
&+ \frac{\lambda + \mu}{4} U_{1,j-1}^{m} - \frac{\lambda + 3\mu}{6} V_{1,j-1}^{m} + \left(\frac{2}{3}\lambda + \mu\right) V_{1,j}^{m} \\
&\left. - \frac{\lambda + \mu}{4} U_{1,j+1}^{m} - \frac{\lambda + 3\mu}{6} V_{1,j+1}^{m} \right].
\end{aligned}
$$

These formulas are very similar to regular-grid finite-differnece ones, but different. They are both second-order accurate in space. However, the FEM requires a less stringent time step. The time step in the FEM is given by $\Delta t < h/V_{\mathrm{p}}$, where V_{p} is the P-wave velocity.

Department of Geological Sciences
University of California, Santa Barbara
Santa Barbara, California 93106
(S.M., R.J.A.)

Institute for Crustal Studies
University of California, Santa Barbara
Santa Barbara, California 93106
(S.M., R.J.A., P.C.L.)

Manuscript received 1 May 2003.